Article:
Zhang, P, Dong, H, Gao, Y et al. (23 more authors) (2023) Many-body Hilbert space scarring on a superconducting processor. Nature Physics, 19 (1). pp. 120-125. ISSN 1745-2473

https://doi.org/10.1038/s41567-022-01784-9

Many-body Hilbert space scarring on a superconducting processor

Pengfei Zhang,[1,*] Hang Dong,[1,*] Yu Gao,[1,*] Liangtian Zhao,[2] Jie Hao,[2] Jean-Yves Desaules,[3] Qiujiang Guo,[1,4] Jiachen Chen,[1] Jinfeng Deng,[1] Bobo Liu,[1] Wenhui Ren,[1] Yunyan Yao,[1] Xu Zhang,[1] Shibo Xu,[1] Ke Wang,[1] Feitong Jin,[1] Xuhao Zhu,[1] Bing Zhang,[4] Hekang Li,[1,4] Chao Song,[1,4] Zhen Wang,[1,4] Fangli Liu,[5] Zlatko Papić,[3] Lei Ying,[1,4,†] H. Wang,[1,4,‡] and Ying-Cheng Lai[6,§]

[1]*Department of Physics, ZJU-Hangzhou Global Scientific and Technological Innovation Center, Interdisciplinary Center for Quantum Information, and Zhejiang Province Key Laboratory of Quantum Technology and Device, Zhejiang University, Hangzhou 310027, China*
[2]*Institute of Automation, Chinese Academy of Sciences, Beijing 100190, China*
[3]*School of Physics and Astronomy, University of Leeds, Leeds LS2 9JT, UK*
[4]*Alibaba-Zhejiang University Joint Research Institute of Frontier Technologies, Hangzhou 310027, China*
[5]*QuEra Computing Inc., Boston, Massachusetts 02135, USA*
[6]*School of Electrical, Computer and Energy Engineering, and Department of Physics, Arizona State University, Tempe, Arizona 85287, USA*

(Dated: November 22, 2022)

Quantum many-body scarring (QMBS) is a recently discovered form of weak ergodicity breaking in strongly interacting quantum systems, which presents opportunities for mitigating thermalisation-induced decoherence in quantum information processing applications. However, the existing experimental realisations of QMBS are based on systems with specific kinetic constrains. Here, we experimentally realise a distinct kind of QMBS by approximately decoupling a part of the many-body Hilbert space in the computational basis. Utilising a programmable superconducting processor with 30 qubits and tunable couplings, we realise Hilbert space scarring in a non-constrained model in different geometries, including a linear chain and a quasi-one-dimensional comb geometry. By reconstructing the full quantum state through quantum state tomography on 4-qubit subsystems, we provide strong evidence for QMBS states by measuring qubit population dynamics, quantum fidelity and entanglement entropy after a quench from initial unentangled states. Our experimental findings broaden the realm of scarring mechanisms and identify correlations in QMBS states for quantum technology applications.

MAIN TEXT

Strongly-coupled quantum systems provide a wealth of opportunities for fundamental physics as well as practical applications that utilise quantum entanglement [1–4]. However, the majority of such systems, even if they are perfectly isolated from the external world, undergo chaotic dynamics and information scrambling [3, 5–8] – the process described by the so-called Eigenstate Thermalisation Hypothesis (ETH) [9–12]. Developing methods to defy the ETH so as to preserve quantum information in long-lived dynamic states has become an important goal of quantum sciences [13].

Recent discovery of quantum many-body scarring (QMBS) [14, 15] – a many-body analog of scarring phenomena in quantum billiards [16] – has shown that certain many-body systems can host non-thermalising eigenstates at high energy densities above their ground state. In such systems, some special initial states have long-lived coherent dynamics, in stark contrast to rapid thermalisation from other initial conditions. This offers a new route for designing non-ergodic dynamics compared to, for example, fine tuning the couplings of the systems to make it integrable, and it avoids the need to strongly disorder the system to drive it into a many-body localized phase [17–20]. Because of their ability to suppress thermalisation for only those selected states, QMBSs are expected to be useful for storing quantum information [14], generating Greenberger–Horne–Zeilinger entangled state [21] and in quantum-enhanced sensing [22]. However, while there has been a proliferation of theoretical studies of QMBS [23–34], the experimental realisations of QMBS remain in short supply. The existing QMBS experiments remain focussed on the kinetically-constrained PXP model [35, 36], which has been effectively realised using Rydberg atoms [13, 37] and ultracold bosons in optical lattices [38]. More recently, ultracold lithium-7 atoms in an optical lattice, which realise the Heisenberg spin model, have been explored as a host of non-thermalising helix states, reminiscent of QMBS [39].

In this article, we report the observation of a new class of QMBS states on a superconducting (SC) processor. In contrast to previous realisations in kinetically constrained Rydberg atom arrays, we design QMBS by weakly decoupling one part of the Hilbert space in the computational basis. Our approach is inspired by the topological structure of the Su-Schrieffer-Heeger (SSH) model of polyacetylene [40], which we utilise to create a nearly decoupled subspace with the structure of the hypercube graph. This subspace gives rise to emergent

* These three authors contributed equally
† leiying@zju.edu.cn
‡ hhwang@zju.edu.cn
§ Ying-Cheng.Lai@asu.edu

QMBS phenomena, including many-body revivals from special initial states residing in the hypercube, as well as the band of scarred eigenstates. Meanwhile, the entire system thermalises due to weak cross couplings between non-nearest-neighbouring qubits. One of the advantages of our SC platform is the tunable XY coupling between qubits (see Methods section for more details) on a 6 by 6 square lattice configuration, which enables us to emulate many-body systems with both one-dimensional (1D) and quasi-1D systems with comb shape. We investigate circuits of up to 30 qubits and 29 couplers, with the Hilbert space dimension $155,117,520$ – far beyond the limits of classical simulation. Measurements of population dynamics and quantum state tomography for entanglement entropy and quantum fidelity provide strong evidence of the emergence of robust QMBS states, as we demonstrate by directly comparing their slow dynamics against conventional thermalising states. Our realisation of a new QMBS paradigm in a solid state SC platform enables a systematic exploration of the fundamental physics of many-body scarring in systems with highly-tunable interactions and configurable lattice topology beyond one spatial dimension.

Mechanism of Hilbert space scarring

Our experiment utilises a two-dimensional SC qubit array [4, 41], shown in Fig. 1**a**, which features high density integration and high degree of controllability over local couplings [42, 43], allowing to emulate different models in a single device. We first consider the "snake"-like qubit layout in Fig. 1**a**. This layout exploits the structure of the SSH chain [40], where the intra-dimer coupling $J_{i,i+1} = J_{\rm a}$ with $i \in$ odd is slightly stronger than the inter-dimer coupling $J_{i,i+1} = J_{\rm e}$ with $i \in$ even. This model is motivated as follows. In the limit $J_{\rm a} \gg J_{\rm e}$, each dimer with one photon behaves as a nearly free two-level system. Hence the SC qubit system is isomorphic to a free spin-1/2 paramagnet. Such a system supports quantum revivals but they are essentially of single-particle origin. When $J_{\rm a}$ and $J_{\rm e}$ are comparable in magnitude, they are in the regime of the SSH model where quench dynamics from fully polarized and Néel initial states has recently been investigated in Refs. [44, 45]. While the Néel state does not display persistent revivals, we will show below that it is possible to identify, based on the graph structure of the Hamiltonian, other initial states that *do* exhibit quantum revivals, even after the interactions break integrability and cause the system to thermalise for most of the other initial states.

We identify candidate QMBS states based on their special location in the Hamiltonian adjacency graph. Each dimer has four states: $|{\rm d}_0\rangle = |00\rangle$, $|{\rm d}_1\rangle = |11\rangle$, $|{\rm d}_+\rangle = |10\rangle$, and $|{\rm d}_-\rangle = |01\rangle$. At half filling, i.e., with the number of photons N equal to half the total number of qubits L, a special class of dimerized states can be identified. These states all have one photon in each dimer (i.e they only contain ${\rm d}_+$ or ${\rm d}_-$) and they form the vertices of a N-dimensional hypercube, with all the edges (i.e., Hamiltonian matrix elements) of equal weight, see Fig. 1**b**. Among these, the collective states $|\Pi\rangle = |{\rm d}_+{\rm d}_-{\rm d}_+{\rm d}_- \cdots\rangle$ and $|\Pi'\rangle = |{\rm d}_-{\rm d}_+{\rm d}_-{\rm d}_+ \cdots\rangle$, have the unique property of only having intra-dimer couplings and they are located at opposite corners of the hypercube in Fig. 1**b**. This suppresses the leakage of information in the states $|\Pi\rangle$ and $|\Pi'\rangle$, with the other states in the hypercube playing the role of a "buffer" area. In order to show that $|\Pi\rangle$, $|\Pi'\rangle$ are *bona fide* QMBSs, it is crucial to demonstrate (i) revivals from $|\Pi\rangle$, $|\Pi'\rangle$ states persist when we break integrability and allow all states to thermalise; (ii) the revivals are a "many-body" effect, i.e., they are not due to the hypercube being trivially decoupled from the rest of the Hilbert space.

Thermalisation in our setup is naturally induced by irregular cross couplings, $J_{\rm x}/2\pi$, experimentally in the range of $[0.3, 1.2]$ MHz – the couplings between two next-nearest neighbour qubits with a physical separation distance $a_{ij} = \sqrt{2}a_0$, where $a_0 \approx 0.8$ mm is the separation distance of two nearest-neighbour qubits. These random couplings break the reflection symmetries of the circuit and thermalise the system, as confirmed by the energy level spacings following the Wigner-Dyson distribution with the parameter $\langle r\rangle \approx 0.53$ – see Supplementary Information (SI). We note, however, that it is also possible to break integrability via translation-invariant perturbations that even *enhance* the revivals from $|\Pi\rangle$, $|\Pi'\rangle$ states, further demonstrating the importance of many-body effects (see SI).

To quantify the impact of the hypercube on the dynamics, note that the sum of the hypercubic-thermal couplings (inter dimer and cross couplings) gives the decay rate Γ of the hypercube to the thermalised parts. The summation of intra hypercubic couplings Δ is given by the number of hypercubic edges, $\Delta = N2^{N-1}J_{\rm a}$. Their ratio Δ/Γ converges to a finite value for different values of $J_{\rm a}/J_{\rm e}$ (see Fig. 1 **b**), which shows that the hypercube is *not* trivially disconnected from the rest of the Hilbert space. At the same time, while other parts of the Hilbert space are frustrated by the irregular $J_{\rm x}$ couplings, no two states within the hypercube are linked by them, thus the hypercubic structure is robust since the cross couplings do not affect the dynamics within it.

Tomographic Measurements

The experimental observations of QMBS states in our SC processor are presented in Fig. 1**c**-**d**. With the high-precision control and readouts, we were able to perform tomography measurements to directly obtain elements of the reduced density matrix $\boldsymbol{\rho}_A$ of the subsystem A. From these, we evaluate the dynamics of the subsystem fidelity, $F_A(t) = {\rm Tr}\left[\boldsymbol{\rho}_A(0)\boldsymbol{\rho}_A(t)\right]$, and bipartite entanglement entropy, $S_{\rm A}(t) = -{\rm Tr}\left[\boldsymbol{\rho}_A(t)\log\boldsymbol{\rho}_A(t)\right]$. The complexity of such measurements grows rapidly with the size of the subsystem A and below we consider A to be four qubits, as schematically illustrated above the panel Fig. 1**c**. We emphasise that although we consider a relatively small subsystem here, the four-qubit fidelity F_A mirrors the behaviour of the full fidelity, as shown numerically in SI. The data points in Fig. 1**c** give, for a 30-qubit chain, the

time evolution of the four-qubit fidelity for the collective state $|\Pi'\rangle$ and two typical thermalising states. The fidelity of the QMBS state exhibits revivals with the period of about 50 ns and the peak value of the first revival can be as high as 0.5, while no such revivals occur for the thermalising states.

In the bottom panel of Fig. 1**c** we measure the time evolution of $S_A(t)$ for QMBS and two conventional thermalising states. Compared to the thermalising states, the scarred dynamics leads to a slightly slower growth of entanglement entropy, superposed with oscillations whose frequency is twice that of fidelity revivals in Fig. 1**c**. This double frequency is due to the fact that the system oscillates between $|\Pi\rangle$ or $|\Pi'\rangle$ states. Thus, entropy is locally minimised or maximised (depending on the choice of subsystem) when the system is near either of these states, while the fidelity only measures the return to the initial state $|\Pi'\rangle$. In our experiment, both scarred and thermalising states ultimately approach the Page entropy, $4\ln(2)$, of the 4-qubit subsystem.

We note that scarring, and in particular the rate of entanglement entropy growth, can be improved by increasing the coupling ratio $J_\mathrm{a}/J_\mathrm{e}$ to 2.5, see Fig. 1**d**. This ratio controls the coupling of the hypercube to the rest of the Hilbert space, as we emphasised above. Furthermore, as shown in SI, some regular perturbations, e.g., a next-next-nearest-neighbour coupling, can efficiently suppress the entropy growth of the scarred state. Similarly, periodic driving of a local potential can significantly enhance the scarred fidelity revivals and inhibit the entropy growth, as also observed in Rydberg atoms [13].

Qubit dynamics beyond the limit of classical simulations

Measurement of the qubit population dynamics is more time-saving than tomography, thus it allows us to further probe thermalisation by randomly choosing many initial product states. The generalised population imbalance is defined as $I(t) = (1/L)\sum_i^L \langle \mathcal{S}_i^z(0)\rangle\langle \mathcal{S}_i^z(t)\rangle$. The imbalance is determined by the overlaps $|\langle E_n|\alpha\rangle|^2$ of energy eigenstates $|E_n\rangle$ with the initial state $|\alpha\rangle$ and the phase factors $\exp(-\mathtt{i}(E_n - E_m)t/\hbar)$, where m, n are eigenstate indices. For a thermalising initial state, the phases are essentially random and the initial state has roughly equal support on all energy eigenstates. Thus, any imbalance rapidly diffuses to a value exponentially small in the system size and it cannot be detected via local operators at late times. By contrast, a QMBS initial state has appreciable overlap only on a *few* eigenstates with phases set to integer multiples of a single frequency. This allows a QMBS state to display a persistent quantum revival even at relatively late times.

The evolution of population imbalance in a 30-qubit chain is shown in Figs. 2**a** and 2**b**, which contrast a QMBS state against a typical thermalising state. The QMBS state exhibits remarkable oscillations which are absent in the thermalising state. The imbalance $I(t)$ is plotted in Figs. 2**c** and 2**d**, which reveal more clearly the differences between two initial states. In general, for the thermalising state, after about 30ns the imbalance has nearly fully decayed to about half a photon in each qubit.

The distinct features of QMBS states can be further highlighted through the overlap between the product states and the eigenstates $|\langle\alpha|E_n\rangle|^2$, which can be represented by the Fourier spectrum of the imbalance, as shown in Figs. 2**e** and 2**f** for the QMBS and thermalising states, respectively. The peak value of the Fourier spectrum $g_\alpha(\omega)$ with the first-order domain eigenstates is $\omega_1/2\pi \approx 21$ MHz. We test 120 random initial product states and find that $g_\alpha^2(\omega = \omega_1)$ of QMBS states are unambiguously distinct from those of conventional thermalising states, as shown in Fig. 2**h**. Note that, for the cases in Figs. 2**a-f**, carrying out the exact simulations is computationally impractical. Instead, the experimental data has been validated by numerical simulation on a smaller system with $L = 20$ (see insets of Figs. 2**c-f**), demonstrating excellent agreement.

The advantage of our experimental system – the tunable effective couplings between two nearest-neighbour qubits – allows us to systematically probe the stability of QMBS states as the ratio of intra- and inter-dimer couplings $J_\mathrm{a}/J_\mathrm{e}$ is varied. As shown in Fig. 2**g**, the numerical and experimental results both indicate that QMBS states consistently emerge in the regime of $J_\mathrm{a}/J_\mathrm{e} \gtrsim 1$. Moreover, even for a chain with uniform nearest-neighbouring couplings ($J_\mathrm{a}/J_\mathrm{e}$=1), the value of $g_\Pi(\omega_1) \approx 0.008$ is significant compared to the average value of thermal states around 0.0035 in Fig. 2**h**. This implies that scarring is not trivially induced by the imbalance between intra-dimer and inter-dimer couplings since this value difference $\sim$ 0.0045 is significantly above the measurement standard deviations given in SI. In the regime of large coupling ($J_\mathrm{a,e}/2\pi > 12$ MHz), the effective Hamiltonian describing our system [see Eq. (3) in the Methods section] is no longer accurate due to the population leakage to couplers. Due to the fast growth of Hilbert space dimension, we did not explore this coupling regime.

To verify the persistence of the QMBS states for different system sizes, we perform measurements on chains of sizes $L = 12$ to 30. The time evolution of the imbalance, the entanglement entropy, and the four-qubit fidelity were found to behave consistently for different system sizes, confirming the robustness of scarring in collective states $|\Pi\rangle$ and $|\Pi'\rangle$. The relatively small variations between the imbalance and the entanglement entropy for different system sizes are due to the difference in the cross couplings and the couplers. The Fourier amplitude $g_\Pi(\omega_1)$ and the fidelity $F_A(t_1)$ at the first revival exhbiti a plateau for $L > 16$, as shown in Fig. 3, whereas for a random initial state these quantities are expected to decrease exponentially with system size. The plateau in the scaling suggests that QMBS states persist in the regime of large system sizes approaching the thermodynamic limit.

Many-body scars on a comb

Our programmable SC circuit allows us to emulate

more complex topology beyond one dimension. We have experimentally studied QMBS states in a comb geometry illustrated in Fig. 4**a**, which consists of a 1D "backbone" decorated with linear "offshoots". Previous studies of quantum comb systems with offshoots of random lengths were shown to exhibit localisation, including "compact" localised states for which the localisation length can vanish along the backbone [29, 46]. In our realisation, we take the offshoots to be of the same length, and we fix $L = N = 20$. We consider each offshoot to be a dimer and, as in the 1D chain, we set the inter-dimer couplings to $J_e/2\pi \simeq -6$ MHz and the intra-dimer ones to $J_a/2\pi \simeq -9$ MHz. In contrast to the chain geometry, the QMBS states in the comb geometry are $|\Theta\rangle = |\mathrm{d}_+\mathrm{d}_+\cdots\rangle$ and $|\Theta'\rangle = |\mathrm{d}_-\mathrm{d}_-\cdots\rangle$. These states are also characteristically distinct from the conventional thermalising states, as revealed by the squared Fourier amplitude in Fig. 4**b**. The striking contrast between a QMBS state and a thermalising state can be seen at a more detailed level from Figs. 4**c**-**e**, which show the time evolution of the imbalance $I(t)$, four-qubit fidelity, and entanglement entropy for $|\Theta'\rangle$ state and a typical thermalising state.

Our experimental results show that the scarring signatures are most striking at intermediate times, while at very late times the system relaxes to a thermal ensemble with nearly maximal entropy. To some extent, one could play with lattice geometry to induce the non-thermal behavior. For example, in the case of the comb lattice structure the model is non-integrable without any perturbation and the entropy growth of the scarred state is much slower than thermalising states for the coupling ratio of $J_a/J_e = 1.5$, as shown in the inset of Fig. 4**e**. In a 2D lattice SC device, the cross couplings are still present and they lead to the scar state fully thermalising by about $300 - 400$ns. Nevertheless, the thermalisation timescale can be significantly extended by periodic driving in the range of experimental capability (see SI).

Discussion and Outlook

In summary, we have presented the first experimental realisation of QMBS states in a solid-state SC platform. Our circuit emulates the effective hard-core Bose-Hubbard model – a model of particles freely hopping on both 1D and quasi-1D lattices, with local interactions. This is in contrast with previous realisations of QMBS in ultracold atomic systems [37, 38], in which the particles' motion is kinetically constrained. Moreover, the underlying mechanism of scarring – approximate decoupling of a hypercube subgraph of the Hilbert space in the computational basis – is distinct from other platforms where QMBS are related to an underlying semiclassical periodic orbit [47]. Our study provides the first in-depth characterisation of QMBS using quantum state tomography on large subsystems. By observing the population dynamics and entanglement entropy, we distinguished the weak ergodicity breaking associated with QMBS initial states from the conventional thermalising states.

The realisation of long-lived quantum states in strongly interacting solid-state systems has notable practical advantages when compared to other mechanisms of ergodicity breaking, such as integrability and many-body localisation (MBL). For example, while integrability is known to be fragile and limited to 1D systems, we demonstrated that QMBSs are robust to various imperfections such as random cross couplings between qubits, and persist beyond 1D systems. On the other hand, while strong ergodicity breaking in MBL systems may offer a more robust way of storing the initial state information for longer times, for applications such as quantum-enhanced sensing and metrology [22], QMBS have the appealing property of extensive multipartite entanglement [48]. In this sense, it is important to note the coupling strength of two qubits (associated with the oscillation frequency of a coherent many-body state $\sim 10^7$ Hz) in our SC platform is significantly larger than other platforms such as 1D Bose gas [49] (only around 10^3 Hz) and Rydberg atom [13] ($\sim 10^6$), which means that the SC platform can process the same quantum information in a shorter time. These advantages of QMBSs in a SC platform could be utilised for more practical quantum sensing and metrology applications. On the fundamental side, our SC devices with the rich palette of tomography-based probes present a convenient setting to probe the interplay of scarred dynamics with localisation on geometries with fractional dimensions and the emergence of diffusive transport in the conventional ETH limit.

ACKNOWLEDGMENTS

The device was fabricated at the Micro-Nano Fabrication Center of Zhejiang University. We acknowledge the support of the National Natural Science Foundation of China (Grants No. 92065204, No. U20A2076, No. 11725419, and No. 12174342), the National Basic Research Program of China (Grants No. 2017YFA0304300), and the Zhejiang Province Key Research and Development Program (Grant No. 2020C01019). The work at Arizona State University is supported by AFOSR through Grant No. FA9550-21-1-0186. Z.P. and J.Y.D. acknowledge support by EPSRC grants EP/R020612/1 and EP/R513258/1, and by Leverhulme Trust Research Leadership Award RL-2019-015. L.Y. is also supported by the Fundamental Research Funds for the Central Universities.

AUTHOR CONTRIBUTIONS STATEMENT

L.Y. proposed the idea. L.Y., Y.-C.L., J.Y.D. and Z.P. developed the theory and numerical simulation. P.Z., H.D. and Y.G. performed the experiment, and H.L. and J.C. fabricated the device supervised by H.W.. L.Z. and J.H. developed the measurement electronics. L.Y., H.W., Y.-C.L. and Z.P. co-wrote the manuscript. All authors contributed to the experimental setup, discussions of the results and development of the manuscript.

COMPETING INTERESTS STATEMENT

The authors declare no competing interests.

[1] Ladd, T. D. *et al.* Quantum computers. *Nature* **464**, 45–53 (2010).

[2] Georgescu, I. M., Ashhab, S. & Nori, F. Quantum simulation. *Rev. Mod. Phys.* **86**, 153–185 (2014).

[3] Mi, X. *et al.* Information scrambling in computationally complex quantum circuits. *Science* **374**, 1479–1483 (2021).

[4] Arute, F. *et al.* Quantum supremacy using a programmable superconducting processor. *Nature* **574**, 505–510 (2019).

[5] Swingle, B., Bentsen, G., Schleier-Smith, M. & Hayden, P. Measuring the scrambling of quantum information. *Phys. Rev. A* **94**, 040302 (2016).

[6] Xu, K. *et al.* Emulating many-body localization with a superconducting quantum processor. *Phys. Rev. Lett.* **120**, 050507 (2018).

[7] Landsman, K. A. *et al.* Verified quantum information scrambling. *Nature* **567**, 61–65 (2019).

[8] Morong, W. *et al.* Observation of Stark many-body localization without disorder. *Nature* **599**, 393–398 (2021).

[9] Deutsch, J. M. Quantum statistical mechanics in a closed system. *Phys. Rev. A* **43**, 2046–2049 (1991).

[10] Srednicki, M. Chaos and quantum thermalization. *Phys. Rev. E* **50**, 888–901 (1994).

[11] Rigol, M., Dunjko, V. & Olshanii, M. Thermalization and its mechanism for generic isolated quantum systems. *Nature* **452**, 854–858 (2008).

[12] Kaufman, A. M. *et al.* Quantum thermalization through entanglement in an isolated many-body system. *Science* **353**, 794–800 (2016).

[13] Bluvstein, D. *et al.* Controlling quantum many-body dynamics in driven Rydberg atom arrays. *Science* **371**, 1355–1359 (2021).

[14] Serbyn, M., Abanin, D. A. & Papić, Z. Quantum many-body scars and weak breaking of ergodicity. *Nature Physics* **17**, 675–685 (2021).

[15] Moudgalya, S., Bernevig, B. A. & Regnault, N. Quantum many-body scars and hilbert space fragmentation: a review of exact results. *Reports on Progress in Physics* **85**, 086501 (2022).

[16] Heller, E. J. Bound-state eigenfunctions of classically chaotic hamiltonian systems: Scars of periodic orbits. *Phys. Rev. Lett.* **53**, 1515–1518 (1984).

[17] Nandkishore, R. & Huse, D. A. Many-body localization and thermalization in quantum statistical mechanics. *Annual Review of Condensed Matter Physics* **6**, 15–38 (2015).

[18] Abanin, D. A., Altman, E., Bloch, I. & Serbyn, M. Colloquium: Many-body localization, thermalization, and entanglement. *Rev. Mod. Phys.* **91**, 021001 (2019).

[19] Guo, Q. *et al.* Stark many-body localization on a superconducting quantum processor. *Phys. Rev. Lett.* **127**, 240502 (2021).

[20] Guo, Q. *et al.* Observation of energy-resolved many-body localization. *Nat. Phys.* **17**, 234–239 (2021).

[21] Omran, A. *et al.* Generation and manipulation of Schrödinger cat states in Rydberg atom arrays. *Science* **365**, 570–574 (2019).

[22] Dooley, S. Robust quantum sensing in strongly interacting systems with many-body scars. *PRX Quantum* **2**, 020330 (2021).

[23] Shiraishi, N. & Mori, T. Systematic construction of counterexamples to the eigenstate thermalization hypothesis. *Phys. Rev. Lett.* **119**, 030601 (2017).

[24] Moudgalya, S., Regnault, N. & Bernevig, B. A. Entanglement of exact excited states of Affleck-Kennedy-Lieb-Tasaki models: Exact results, many-body scars, and violation of the strong eigenstate thermalization hypothesis. *Phys. Rev. B* **98**, 235156 (2018).

[25] Schecter, M. & Iadecola, T. Weak ergodicity breaking and quantum many-body scars in spin-1 XY magnets. *Phys. Rev. Lett.* **123**, 147201 (2019).

[26] Moudgalya, S., Bernevig, B. A. & Regnault, N. Quantum many-body scars in a Landau level on a thin torus. *Phys. Rev. B* **102**, 195150 (2020).

[27] McClarty, P. A., Haque, M., Sen, A. & Richter, J. Disorder-free localization and many-body quantum scars from magnetic frustration. *Phys. Rev. B* **102**, 224303 (2020).

[28] van Voorden, B., Minář, J. c. v. & Schoutens, K. Quantum many-body scars in transverse field Ising ladders and beyond. *Phys. Rev. B* **101**, 220305 (2020).

[29] Hart, O., De Tomasi, G. & Castelnovo, C. From compact localized states to many-body scars in the random quantum comb. *Phys. Rev. Research* **2**, 043267 (2020).

[30] Zhao, H., Vovrosh, J., Mintert, F. & Knolle, J. Quantum many-body scars in optical lattices. *Phys. Rev. Lett.* **124**, 160604 (2020).

[31] Kuno, Y., Mizoguchi, T. & Hatsugai, Y. Flat band quantum scar. *Phys. Rev. B* **102**, 241115 (2020).

[32] O'Dea, N., Burnell, F., Chandran, A. & Khemani, V. From tunnels to towers: Quantum scars from lie algebras and q-deformed lie algebras. *Phys. Rev. Research* **2**, 043305 (2020).

[33] Desaules, J.-Y., Hudomal, A., Turner, C. J. & Papić, Z. Proposal for realizing quantum scars in the tilted 1D Fermi-Hubbard model. *Phys. Rev. Lett.* **126**, 210601 (2021).

[34] Ren, J., Liang, C. & Fang, C. Quasisymmetry groups and many-body scar dynamics. *Phys. Rev. Lett.* **126**, 120604 (2021).

[35] Fendley, P., Sengupta, K. & Sachdev, S. Competing density-wave orders in a one-dimensional hard-boson model. *Phys. Rev. B* **69**, 075106 (2004).

[36] Lesanovsky, I. & Katsura, H. Interacting Fibonacci anyons in a Rydberg gas. *Phys. Rev. A* **86**, 041601 (2012).

[37] Bernien, H. *et al.* Probing many-body dynamics on a 51-atom quantum simulator. *Nature* **551**, 579–584 (2017).

[38] Su, G.-X. *et al.* Observation of unconventional many-body scarring in a quantum simulator arXiv:2201.00821

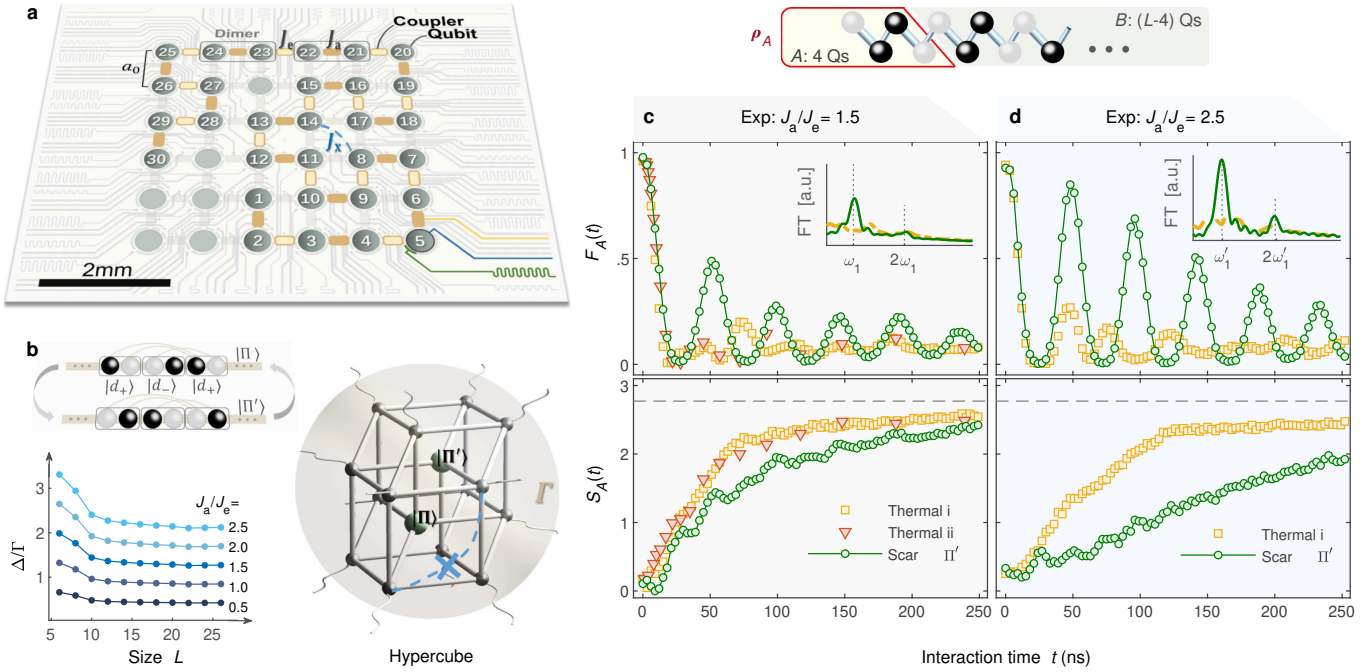

FIG. 1. **Experimental setup and identification of QMBS states via quantum state tomography. a**, Experimental superconducting circuit of Device I with qubits and couplers in a square geometry. Light gray dashed rectangles represent dimers that constitute the chain with intra coupling J_a, inter coupling J_e, and small cross coupling J_x. **b**, Left upper: A schematic illustration of the dynamics of the collective dimer states $|\Pi\rangle$ and $|\Pi'\rangle$. Left lower: Numerics of the ratio Δ/Γ as a function of the system size L for different ratios of J_a/J_e, with $J_x/2\pi$ in the range of $[0.3, 1.2]$ MHz. Right: a 4-dimensional hypercube in the Hilbert space. **c**, Quantum state tomography for the four-qubit fidelity $F_A(t)$ and entanglement entropy $S_A(t)$ in a 30-qubit chain for thermalising initial states, $|0101\ldots0110\rangle$ (labelled as "i") and $|01001\ldots100110110\rangle$ ("ii") and the QMBS state Π' (green). The couplings are $J_a/2\pi = 1.5J_e/2\pi \simeq -9$ MHz. The inset shows the Fourier transform of the four-qubit fidelity with the peak at $\omega_1/2\pi \approx 21$ MHz. The dashed grey line in the bottom panel represents the maximal thermal entropy for the subsystem, approaching to $4\ln 2$. **d**, Same as **c**, but for different couplings $J_a/2\pi = 2.5J_e/2\pi \simeq -10$ MHz from Device II and $\omega_1'/2\pi \approx 22$ MHz. The schematic above panels (**c**, **d**) illustrates the bipartition of the system.

(2022).

[39] Jepsen, P. N. *et al.* Long-lived phantom helix states in Heisenberg quantum magnets. *Nature Physics* **18**, 899–904 (2022).

[40] Su, W. P., Schrieffer, J. R. & Heeger, A. J. Solitons in polyacetylene. *Phys. Rev. Lett.* **42**, 1698–1701 (1979).

[41] Wu, Y. *et al.* Strong quantum computational advantage using a superconducting quantum processor. *Phys. Rev. Lett.* **127**, 180501 (2021).

[42] Krantz, P. *et al.* A quantum engineer's guide to superconducting qubits. *Applied Physics Reviews* **6**, 021318 (2019).

[43] Blais, A., Grimsmo, A. L., Girvin, S. M. & Wallraff, A. Circuit quantum electrodynamics. *Rev. Mod. Phys.* **93**, 025005 (2021).

[44] Jafari, R. & Johannesson, H. Loschmidt echo revivals: Critical and noncritical. *Phys. Rev. Lett.* **118**, 015701 (2017).

[45] Najafi, K., Rajabpour, M. A. & Viti, J. Return amplitude after a quantum quench in the XY chain. *Journal of Statistical Mechanics: Theory and Experiment* **2019**, 083102 (2019).

[46] Maimaiti, W., Andreanov, A., Park, H. C., Gendelman, O. & Flach, S. Compact localized states and flat-band generators in one dimension. *Phys. Rev. B* **95**, 115135 (2017).

[47] Ho, W. W., Choi, S., Pichler, H. & Lukin, M. D. Periodic orbits, entanglement, and quantum many-body scars in constrained models: Matrix product state approach. *Phys. Rev. Lett.* **122**, 040603 (2019).

[48] Desaules, J.-Y., Pietracaprina, F., Papić, Z., Goold, J. & Pappalardi, S. Extensive multipartite entanglement from su(2) quantum many-body scars. *Phys. Rev. Lett.* **129**, 020601 (2022).

[49] Malvania, N. *et al.* Generalized hydrodynamics in strongly interacting 1d bose gases. *Science* **373**, 1129–1133 (2021).

METHODS

Device–We use a superconducting quantum processor in a flip-chip package, which hosts a square of 6×6 transmon qubits (Q_i) with 60 couplers (Q_c), each inserted in-between two neighbouring qubits, as shown in Fig. 1**a**. Each qubit (coupler) is a quantum two-level system with ground state $|0\rangle$ and excited state $|1\rangle$, whose energy separation can be dynamically tuned in the frequency range $4.3-4.8$ GHz ($4.9-6.0$ GHz). Each qubit has individual

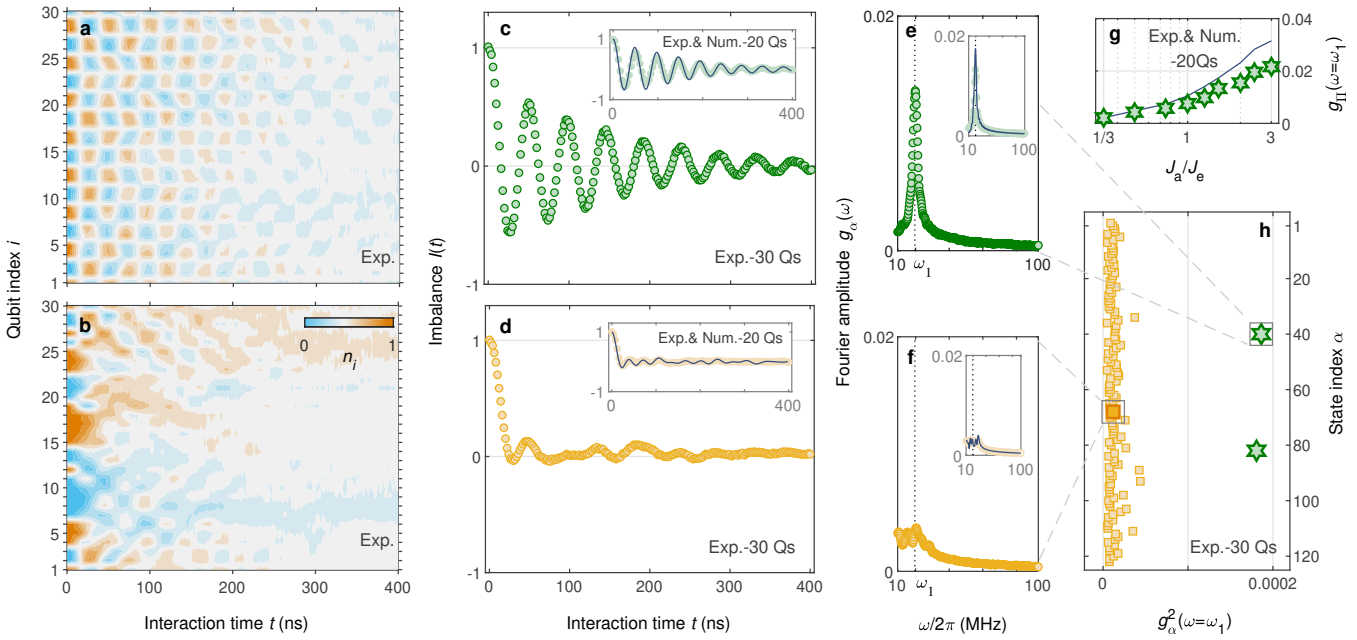

FIG. 2. **Experimentally observed qubit dynamics.** (Device I) **a**,**b**, Contour diagrams of the experimental qubit population as a function of the interaction time for a QMBS and a rapid thermalising state, respectively. **c**,**d**, Generalised imbalance $I(t)$ extracted from plots **a**,**b** as a function of the interaction time. Insets: imbalance dynamics from experiments (dots or circles) and numerical simulations (solid curves) in a 20-qubit chain. **e**,**f**, The Fourier transformation amplitude of the imbalance in (**c**,**d**), which characterizes the squared overlap between the initial states and the energy eigenstates. The time window for the fast Fourier transform is extended to 4 μs with zero padding. **g**, Fourier peak as a function of the coupling ratio J_a/J_e in a chain of $L = 20$ from experimental measurements (green hexagrams) and numerical simulations (solid curve). **h**, The squared Fourier amplitude $g^2_\alpha(\omega = \omega_1)$ of $|\alpha\rangle$ for 120 randomly chosen initial product states, including two QMBS states (green hexagrams) that clearly stand out from the rest of thermalising product states (yellow squares). The simulation parameter values in panels **c-f** are $J_a/2\pi = -9.3$ MHz, $J_e/2\pi = -6.1$ MHz and $J_x/2\pi \in [0.3, 1.2]$ MHz.

microwave (XY) and flux (Z) controls and it is capacitively coupled to a readout resonator for state discrimination. Each coupler has an individual flux (Z) control and remains in the ground state during the experiment. We use high-precision synchronized analog signals to control the qubits and couplers, with microwave pulses for qubit XY rotations and state readout, and square flux pulses for tuning the qubit and coupler frequencies. A complete experimental sequence consists of three stages: (1) state preparation where single-qubit $\boldsymbol{\pi}$ pulses are applied to half of the qubits, (2) multiqubit interaction stage where the nearest neighbouring qubit couplings are programmed by adjusting the couplers' frequencies, and (3) the measurement stage where all qubits are jointly read out. The values of the relevant qubit parameters such as the qubit operation frequencies, energy relaxation times (with mean about 50 μs) and single-qubit randomized benchmarking fidelities (with mean about 0.993) can be found in Table S1 of SI.

Effective model–We derive the effective spin-1/2 XY model for our experimental superconducting processor. The full Hamiltonian of the superconducting circuit-QED system with both qubits and couplers is given by [42, 50]

$$\begin{aligned}\mathcal{H}_{\rm full}/\hbar = &\sum_i \left(\omega_i \mathcal{S}_i^+\mathcal{S}_i^- + \frac{\eta_i}{2}\mathcal{S}_i^+\mathcal{S}_i^+\mathcal{S}_i^-\mathcal{S}_i^-\right)\\ &+\sum_c \left(\omega_c \mathcal{S}_c^+\mathcal{S}_c^- + \frac{\eta_c}{2}\mathcal{S}_c^+\mathcal{S}_c^+\mathcal{S}_c^-\mathcal{S}_c^-\right)\\ &+\sum_{\langle i,j\rangle} g_{ij}(\mathcal{S}_i^-\mathcal{S}_j^+ + \mathcal{S}_j^-\mathcal{S}_i^+)\\ &+\sum_{\langle i,c\rangle} g_{ic}(\mathcal{S}_i^+\mathcal{S}_c^- + \mathcal{S}_i^-\mathcal{S}_c^+),\end{aligned} \tag{1}$$

where ω_i (ω_c) is the frequency of the ith qubit (c's coupler), $\mathcal{S}_i^+$ ($\mathcal{S}_i^-$) is the creation (annihilation) operator of Q_i, g_{ij} (g_{ic}) is the coupling strength between Q_i and Q_j (Q_c), and the rotating wave approximation is imposed on the qubit-coupler and qubit-qubit couplings. The subscripts "i, j" and "c" represent the indices of qubits and couplers, respectively. $\langle i, j\rangle$ or $\langle i, c\rangle$ stands for a nearest-neighbour qubit-qubit or qubit-coupler pair. In experiments, the anharmonicity η_i is much larger than the couplings between the nearest neighbouring qubits (typically $\eta_i/g_{ij} > 50$), so the full Hamiltonian (1) can be reduced

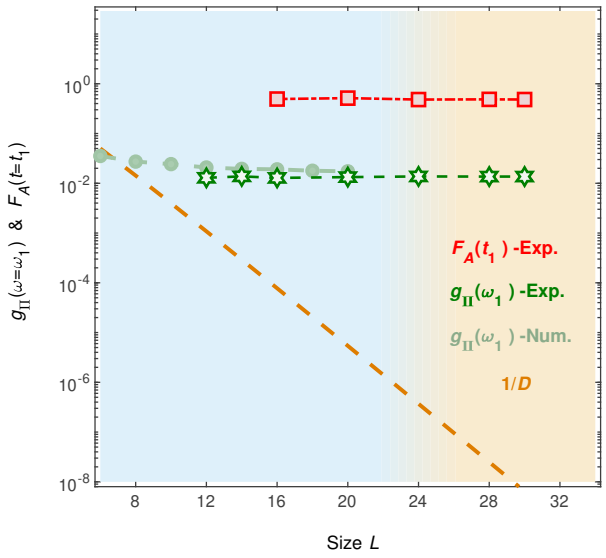

FIG. 3. **Scaling behavior**. Scaling of the first revival peak $F_A(t_1 \approx 52\text{ns})$ of the subsystem A, Fourier amplitude $g_{\Pi}(\omega_1)$, and the inverse Hilbert space dimension $1/D$ versus the system size for $J_a/2\pi \simeq -9$ MHz and $J_e/2\pi \simeq -6$ MHz. The light blue area denotes the regime where classical simulations using the exact diagonalization method are feasible.

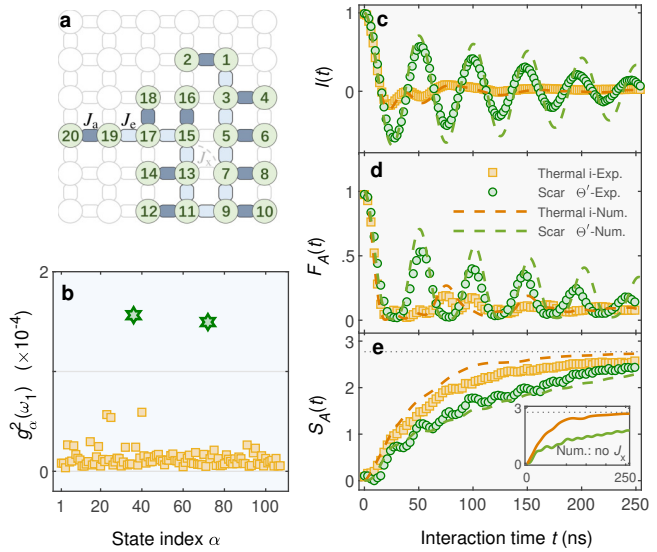

FIG. 4. **QMBS states in a comb tensor system. a**, The comb tensor topology on the superconducting processor (Device I) with $L = 20$ qubits. **b**, Squared Fourier amplitude $g_\alpha^2(\omega = \omega_1)$ for randomly chosen initial product states. The QMBS states (green hexagrams) are characteristically distinct from the conventional thermalising product states. **c-e**, Dynamics of the imbalance, four-qubit fidelity, and four-qubit entanglement entropy for the state $|\Theta'\rangle$ (green circles) and a randomly chosen product state $|00111000111010011001\rangle$ (yellow squares,labelled as "i") for a 20-qubit comb. Dashed curves denote the numerical results. Inset to panel **e** shows the numerical result in the case without cross couplings J_x, where the scarred state shows a much slower entropy growth from the thermalising state. The couplings are tuned to $J_a/2\pi \simeq -9$ MHz and $J_e/2\pi \simeq -6$ MHz.

to the spin-1/2 XY Hamiltonian:

$$\mathcal{H}/\hbar = \sum_i \omega_i \mathcal{S}_i^+ \mathcal{S}_i^- + \sum_c \omega_c \mathcal{S}_c^+ \mathcal{S}_c^- + \sum_{\langle i,j\rangle} g_{ij}(\mathcal{S}_i^- \mathcal{S}_j^+ + \mathcal{S}_j^- \mathcal{S}_i^+) + \sum_{\langle i,c\rangle} g_{ic}(\mathcal{S}_i^+ \mathcal{S}_c^- + \mathcal{S}_i^- \mathcal{S}_c^+). \tag{2}$$

We apply the Schrieffer-Wolff transformation $\mathcal{U} = e^{\mathcal{W}}$ to the Hamiltonian with

$$\mathcal{W} = \sum_c \sum_i \frac{g_{ic}}{\Delta_{ic}}(\mathcal{S}_i^+ \mathcal{S}_c^- - \mathcal{S}_i^- \mathcal{S}_c^+),$$

since all qubits are far detuned from the couplers with $|\Delta_{ic}| = |\omega_i - \omega_c| \gg |g_{ic}|$. The effective Hamiltonian can then be approximated as

$$\mathcal{H}_{\text{eff}}/\hbar \approx \sum_{\langle i,j\rangle} J_{ij}(\mathcal{S}_i^- \mathcal{S}_j^+ + \mathcal{S}_i^+ \mathcal{S}_j^-) + \sum_i \Omega_i \mathcal{S}_i^+ \mathcal{S}_i^-, \tag{3}$$

where the effective coupling strength and transition frequencies are given by

$$J_{ij} = g_{ij} + \sum_c g_{ic} g_{jc} \Big[\frac{1}{\Delta_{ic}} + \frac{1}{\Delta_{jc}}\Big], \tag{4}$$

$$\Omega_i = \omega_i + \sum_c \frac{g_{ic}^2}{\Delta_{ic}}, \tag{5}$$

respectively. The strength of the indirect coupling can be tuned by adjusting the coupler frequency, so the effective coupling strength $J_{ij}/2\pi$ can be dynamically tuned over a wide range, typically in $[-15, 1]$ MHz.

In our experiment, the chain and comb structures are formed by a snake-like qubit layout on a square-lattice device, hence the dominant cross coupling cannot be neglected. The cross perturbation Hamiltonian is given by

$$\mathcal{H}_x/\hbar = \sum_{R_{ij}=\sqrt{2}a_0} J_x(i,j)\left[\mathcal{S}_i^+ \mathcal{S}_j^- + \mathcal{S}_j^+ \mathcal{S}_i^-\right], \tag{6}$$

where $R_{ij} = |\mathbf{r}_i - \mathbf{r}_j|$ is the separation distance of a qubit pair {i,j}. The couplings are in the range $J_x(i,j)/2\pi \in [0.3, 1.2]$ MHz and their measured values are given in SI. The magnitude of this perturbation is sufficiently large to break integrability of the model, as demonstrated numerically in SI.

Experimental sequence–Experimentally, we prepare a set of product states as initial states and measure the final states of all qubits as a function of the interaction time (see pulse sequence illustrated in Extended Data Fig. 1. A typical experimental session starts by preparing the initial product state of all qubits: each qubit Q_i is biased from its sweet spot to the corresponding idle frequency, where we apply single-qubit XY ro-

tations. To prepare a high-fidelity state, during this period the couplers are tuned such that the net couplings between neighbouring qubits are turned off. To switch on the interactions among the qubits, we bias all qubits to the interaction frequency and tune the coupler frequencies to turn on the couplings between neighbouring qubits. After the interaction process, we bias all qubits to their readout frequencies for measurements. All directly measured qubit occupation probabilities are corrected to eliminate the measurement errors.

Numerics– We use the exact diagonalization method to numerically solve the eigenvalue problem and simulate the dynamics of the system. The basis of the Hamiltonian matrix is spanned by product states $|\alpha\rangle = |z_1\rangle \otimes |z_2\rangle \otimes |z_3\rangle \otimes \cdots \otimes |z_L\rangle$, also written as $|z_1 z_2 z_3 \cdots z_L\rangle$, where $z_j = 0$ or 1 represents jth qubit at state $|0\rangle$ or $|1\rangle$. The elements of Hamiltonian matrix are written as

$$H_{\alpha\beta} = \langle\alpha|\mathcal{H}|\beta\rangle, \tag{7}$$

where α, β denote the index of basis product states. Then, the eigenstate $|n\rangle$ and its eigenvalue E_n can be numerically solved from this Hamiltonian matrix. They are used to compute the spectrum-related quantities, such as entanglement entropy and overlap, as well as the dynamics of qubit populations, imbalance and wavefunction fidelity.

The Hamiltonian matrix is exponentially large in the number of qubits and to facilitate its diagonalization, we decompose it into smaller sectors based on the symmetries of the model. For our spin-1/2 XY model with open boundary condition, these include particle conservation, reflection, and symmetries. The original basis can be naturally divided into $L + 1$ uncoupled sectors, which conserve particle number. The numerics throughout the paper is for the particle number equal to half of the system size. Furthermore, to construct subspaces invariant under the reflection and symmetries, we define a new set of basis states

$$|\tilde{\alpha}(r, z)\rangle = \frac{1}{\sqrt{N_\alpha}} (1 + r\mathcal{R}) (1 + z\mathcal{Z})|\alpha\rangle. \tag{8}$$

Here, $r = \pm 1$ and $z = \pm 1$ are the eigenvalues of reflection- and inversion-symmetry generators $\mathcal{R}$ and $\mathcal{Z}$, respectively. N_α is the normalization factor. The cross couplings J_{x} break the reflection symmetry and the basis in this case is given by $|\tilde{\alpha}(z)\rangle = \left((1 + z\mathcal{Z}) / \sqrt{N_\alpha}\right) |\alpha\rangle$.

We note that exact diagonalization is not the only numerical method available for this problem. However, alternative options are not well-suited for studying quantum many-body scarring in large systems. Krylov- and Matrix-Product States (MPS) based methods could potentially access the dynamics from Π or Π' states for a few more qubits than 24. However, to show scarring requires studying the dynamics from a large number of initial states. In contrast to exact diagonalization, these two methods require an independent computation for each initial state. Furthermore, for MPS methods it would also be costly to simulate the dynamics of thermalising states as their entanglement entropy very quickly reaches the Page value. This would limit the simulation to a relatively short time, as the bond dimension of the MPS (and so the computational resources needed) required to capture the dynamics faithfully would rapidly become large.

DATA AVAILABILITY

The data that support the findings of this study are available in https://doi.org/10.5518/1204.

CODE AVAILABILITY

All relevant source code is available from the corresponding author upon reasonable request.

[50] Neill, C. *et al.* A blueprint for demonstrating quantum supremacy with superconducting qubits. *Science* **360**, 195–199 (2018).